Review

Electrochemical Impedance Spectroscropy Study on the Behavior of Reinforced Concrete Elements under Loading

Belén Díaz [ID], X. Ramón Nóvoa *[ID] and Carmen Pérez [ID]

CINTECX, Universidade de Vigo, Encomat Group, 36310 Vigo, Spain
* Correspondence: rnovoa@uvigo.es; Tel.: +34-98-681-2213

Abstract: Concrete is a material of porous nature that, when humidified, becomes an ionic conductor whose apparent conductivity depends on the ionic load (typically based on OH^-, Ca^{2+}, Na^+, and K^+) and the amount of available free water. Under conditions of partial pore-saturation, the amount of free water can be modulated by an external load, which leads to observable changes in electrical properties such as conductivity and capacitance. Moreover, metallic reinforcements, either as bars or fibers, represent an additional parallel conduction path but of an electronic nature in this case. The free water develops a double-layer capacitance structure at the metallic interfaces, with associated charge-transfer resistance, representing an additional contribution to the capacitive behavior that can be modulated with an external load. The dependence that the electrical and/or ionic conducting properties of concrete and reinforced concrete elements have on the available free water makes them suitable for transductors in various sensing and self-sensing applications discussed in the text.

Keywords: cement; concrete; impedance; sensing

1. Introduction

The use of electrochemical impedance spectroscopy, EIS, in the characterization of the steel–concrete system started in the early 1980s with the pioneering work by Dawson et al. [1]. Although the main interest in using EIS was always to obtain the charge-transfer resistance (or the polarization resistance, R_p) exploring the mHz frequency range, Dawson's work already showed the presence of some response in the high-frequency range (beyond 1–10 kHz), which was initially attributed to some dielectric characteristics of the steel–concrete interface. By the 1990s, other authors [2–4] had published the results claiming the possibility to characterize the concrete microstructure by means of A.C. techniques. The debate was intense throughout that decade on the origin of the dielectric feature in the kHz–MHz range [5–10], but now there is a consensus on the contribution of water to pore walls [11,12].

Figure 1 shows the overall picture of the whole system where along more than nine frequency decades, the different phenomena can be differentiated. The microstructure of the ceramic in the MHz–kHz range, the oxides layer in the kHz domain [13], and the redox processes are associated with the Faradaic reactions (corrosion and transformations in the oxides layer) at frequencies in the Hz–mHz and below.

A crucial aspect of EIS measurements in cementitious materials is the geometry to produce homogeneous electric field distribution through the sample and on the working electrode. Simple geometries (parallel plate or cylindrical) have been recommended [14,15] to obtain reliable parameters (resistances and capacitances). As it concerns the frequency measurements in the kHz–MHz domain, the two-electrode parallel plate electrode arrangement, with appropriate guarding, is mandatory to avoid the contribution of stray capacitances [16,17].
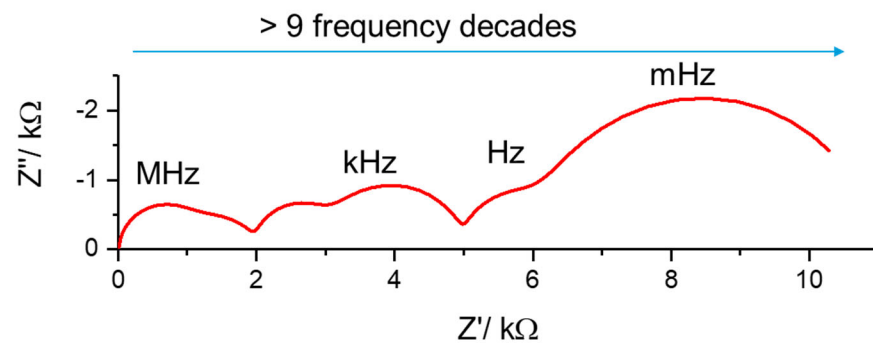
Figure 1. Idealized Nyquist EIS plot showing the extensive range of frequencies in which the various phenomena present in the steel–concrete system can be observed.

The concept of self-monitoring concrete was introduced in the nineties by D.D.L. Chung [18], related to changes in resistivity of the cementitious material (with or without fibers) with external load or local relative humidity changes. The research in the field became very dynamic, and self-sensing elements were fabricated with various binders and fillers, including FeOx, carbon black, carbon nanotubes, or carbon fibers [19–23]. With the fillers being of an electronically conducting character, their sensing ability to load lies in their concentration approaching the percolation threshold, thus measuring conductivity changes.

The importance of water content in self-monitoring devices was less studied [24–26], perhaps due to the poor understanding of the water contribution to the overall capacitance of the system [27]. Thus, this review focuses mainly on this aspect.

2. The States of Water in Porous Materials

As aforementioned, the high-frequency region of the impedance spectra shall be explored under a well-defined geometrical arrangement of the electrodes. Depending on the purpose of the study, two experimental approaches are conceivable: a permeation-type cell and a parallel plate. The former option is suitable for obtaining the material's ionic conductivity and relevant parameters such as the chloride diffusion coefficient [28] after proper correction for the current distribution [16]. The latter is ideal for capacitance measurements and gathering information related to the microstructure [29].

Figure 2 shows the characteristic impedance plots in the high frequency domain obtained when employing the permeation cell arrangement [30] (Figure 2a) and the insulated parallel plate [29] (Figure 2b). The presence of two time constants (RC associations) is evident in Figure 2a. This feature is less apparent in Figure 2b. Still, the transformation into equivalent capacitance (via Equation (1)) produces Figure 2d where two capacitances can be distinguished, the high and low-frequency limits of the plot, according to Equation (2).

$$C(\omega) = (j\omega(Z(\omega) - R_e))^{-1} \tag{1}$$

$$C(\omega) = C_1 + \frac{C_2}{\left(1 + (j\omega R_2 C_2)^\alpha\right)^\beta} \tag{2}$$

In Equation (1), ω is the angular frequency ($2\pi f$, f in Hz), $j = \sqrt{-1}$, R_e is the uncompensated resistance (typically the contact impedance), and $Z(\omega)$ is the measured impedance at frequency ω.

Equation (2) describes the Figure 2d plot, with a high-frequency capacity limit, C_1, and a low-frequency capacity limit corresponding to $C_1 + C_2$. The dispersion parameters α and β are directly linked to the distribution of the pore families [29]. Formally, in the case of $\alpha = 1$ and $\beta = 1$, the dielectric dispersion is known as the Debye type; for $0 < \alpha < 1$ and $\beta = 1$, as the Cole–Cole type; and for $\alpha = 1$ and $0 < \beta < 1$, as the Cole–Davidson type.
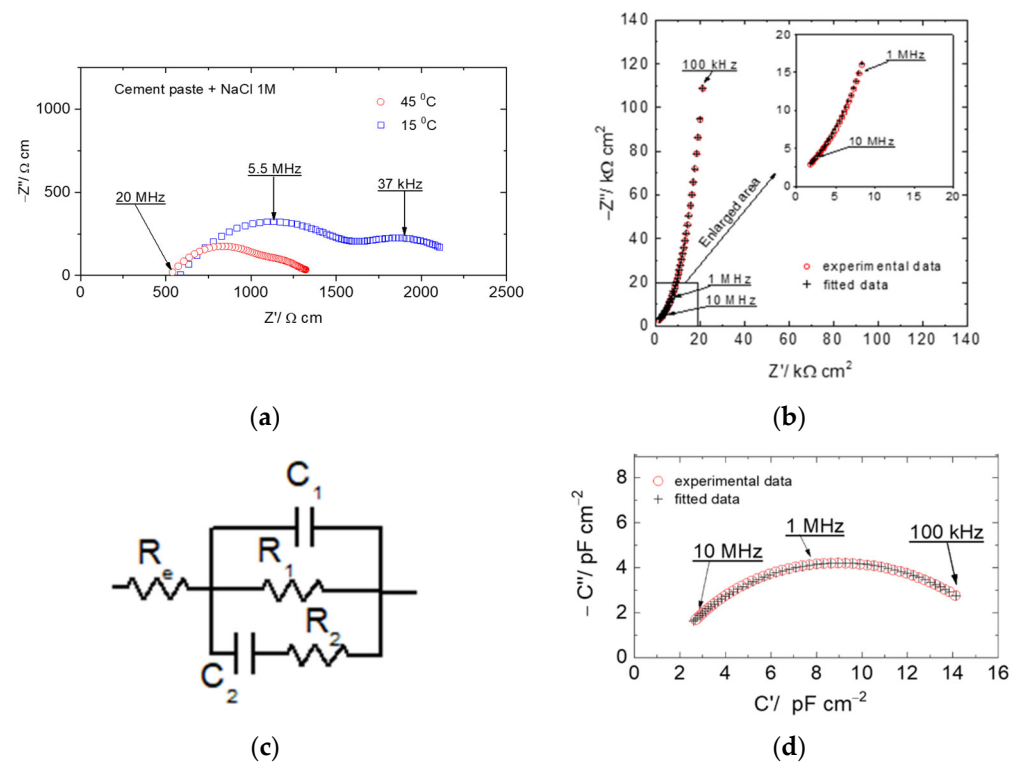
Figure 2. Typical impedance plots for cement paste samples using (**a**) a permeation cell [30] and (**b**) a parallel plate with insulated surfaces [29]. (**c**) Equivalent electrical circuit (see text for details). (**d**) Transformation of data in (**b**) using Equation (1).

Equation (2) also corresponds to the equivalent capacitance of the circuit depicted in Figure 2c, once the contact resistance, R_e, and the percolation resistance, R_1, are removed. C_1 accounts for the geometrical capacitance (according to Equation (3)), and R_2C_2 is a Maxwell-type relaxation element linked to the ionic motion and double layer capacitance at the pore's wall [29]. The number of Maxwell-type relaxation elements is variable depending on the system microstructure. It is easy to see that the only difference between both types of measurement comes from the intrinsic difference between them: the percolation, represented by R_1 in Figure 2c. The two capacitances are present no matter the experimental arrangement.

$$\text{C} = \varepsilon\varepsilon_0(S/d) \qquad (3)$$

Equation (3) corresponds to the capacity of a flat condenser where the ratio *S/d* (the surface over the distance between plates) is the geometrical factor, ε is the relative permittivity, and ε_0 is the vacuum permittivity ($8.85\ 10^{-14}\ \text{Fcm}^{-1}$).

Impedance plots similar to that in Figure 2a were also found for other porous structural materials such as stones during chloride extraction experiments [31]. In addition, functional porous materials such as organic coatings also showed a high-frequency feature in a lower frequency range, and a high degree of overlapping of the two capacitive arcs, as shown in Figure 3a, where the coating's water uptake was followed as a function of immersion time [32]. Interestingly, with organic coatings, it is possible to simultaneously record the high frequency capacitance and the mass gain using a quartz crystal microbalance. An example of those results appears in Figure 3b [33]. The effective contribution of the mass gain (due to water uptake) to the recorded capacitance decreases as mass gain increases. This fact suggests that the commonly employed method to evaluate water uptake [34], the Brasher–Kingsbury equation (Equation (4)), has limited domain of applicability.
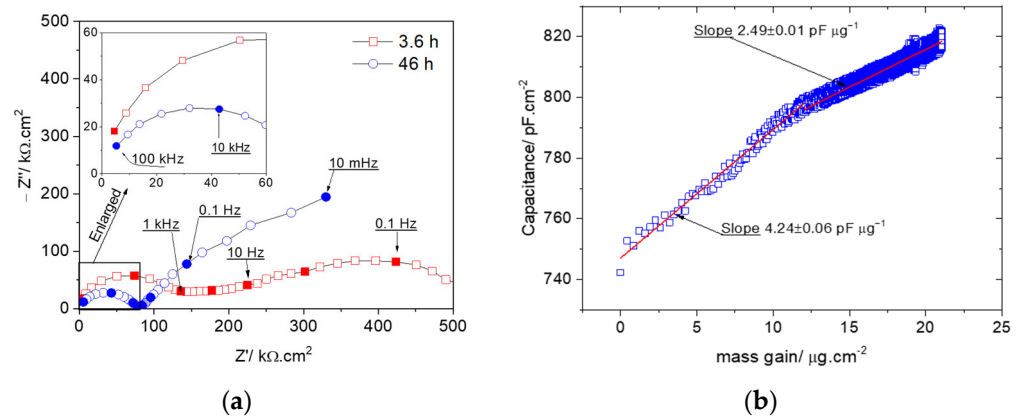
Figure 3. (**a**) Typical impedance plots obtained during a coating's water uptake [32]. (**b**) Relationship between the high frequency coating capacitance and the mass gain (water uptake) [33].

$$\chi_v = 100 \frac{log\left(c_m(t)/c_m(t=0)\right)}{log(\varepsilon_w)} \tag{4}$$

In Equation (4), χ_v is the water uptake at time t (fraction volume), $c_m(t)$ is the capacitance at time t, $c_m(t=0)$ is the initial coating capacitance (air-filled porosity), and ε_w is the dielectric constant of water, 76.6 at 30 °C.

From the inspection of Figure 3b, it is clear that the application of Equation (3) requires considering different values for the dielectric constant of water, which will give rise to other Maxwell-type relaxation elements in Figure 2c. In this Figure, C_1 is the only one related to the geometry and thus to the dielectric constant of the solid matrix (via Equation (3) in parallel plate configuration).

3. The Dielectric Permittivity of Water

Domestic microwave ovens work at 2.45 GHz, close to the characteristic frequency of the water molecule rotation in liquid water, as shown in Figure 4. However, for ice, the characteristic frequency is six orders of magnitude less and does not absorb energy in the GHz. The rotation of the bound water molecule in ice is much slower (one million times) than in liquid water. Thus, in the frequency range explored in cement (around MHz), liquid water will show a dielectric constant of about 80, while bound water will remain below 10 (in the high frequency limit), as shown in Figure 4.
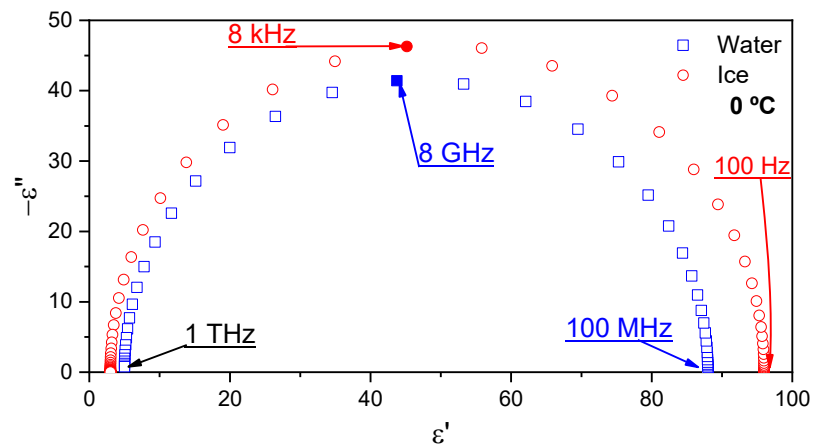

Figure 4. Cole–Cole plot showing the real, ε', and imaginary, ε'', parts of the dielectric permittivity of water and ice, both at 0 °C. Reconstructed from data in [35].

The activation energy corresponding to the rotation (relaxation process) can also be taken as an indicator of the easiness of rotating. Figure 5a shows that the activation energy is 0.56 eV for water in ice and 0.165 eV for liquid water. Figure 5b corresponds to the R_2C_2 time constant obtained for cement paste specimens (from [30]). The calculated activation energy is 0.25 eV, which reveals that water in cement paste does not behave as free water. Its motion is somehow restricted due to interaction with pore walls (in gel pores) or hydrogen bonding in interlamellar spaces.
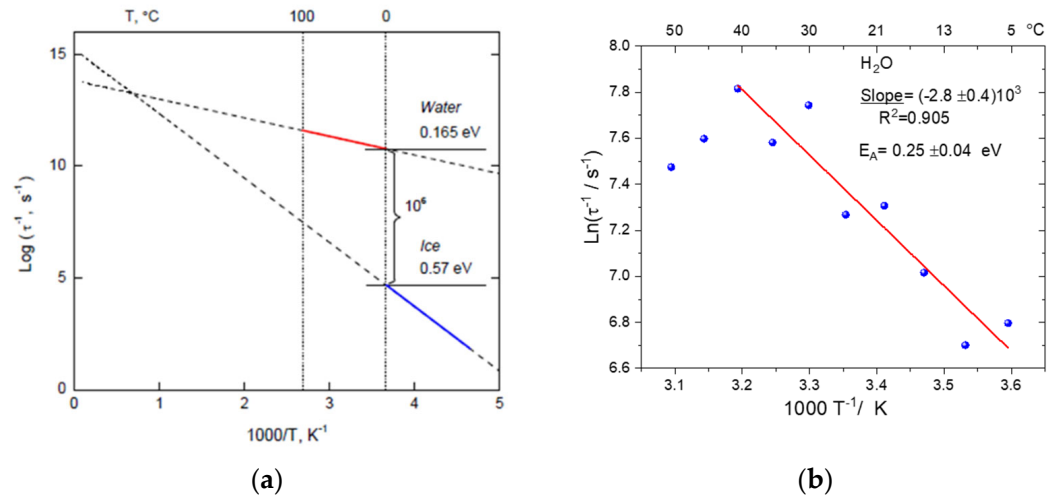

(a)   (b)

Figure 5. (**a**) The Arrhenius plot for the inverse relaxation times of water and ice, showing the corresponding activation energies, reprinted with permission from Ref. [35]. (**b**) The Arrhenius plot for the inverse of the R_2C_2 time constant of mortar specimens, reconstructed from data in [30].

4. The Self-Sensing Capability of Cementitious Materials

The self-sensing capability usually refers to the possibility of detecting changes in load, RH, or crack formation. The principles of those capabilities are presented in this section.

4.1. Bare elements

4.1.1. Load Sensing

In the early 80's, Sierra [36], based on IR and NMR spectrometry, proposed a model illustrating the water distribution in the C-S-H gel. The state of the structuring of this water bound to hydrates shows that it contributes to a certain extent to the cohesion of cement pastes, based on hydrogen bonds, as shown in Figure 6a. The model is based on a previous one by Feldman [37] that considers interlayer water as an stabilizing agent that can be reversibly removed under loading, as depicted in Figure 6b.

The sliding between C-S-H sheets due to loading results in breaking hydrogen bonds and forming free water. As discussed in the previous section, the breakdown of hydrogen bonds should lead to increased available free water, which will increase capacitance (the dielectric constant increases).

Figure 7a shows the low-frequency limit of the complex capacitance increases (C_2 increases) upon loading, which agrees with the rise of the water dielectric constant due to the breakdown of hydrogen bonds. Interestingly, the process is reversible, as Figure 7b shows. However, a lack of reversibility will occur under plastic deformation with microcrack development.
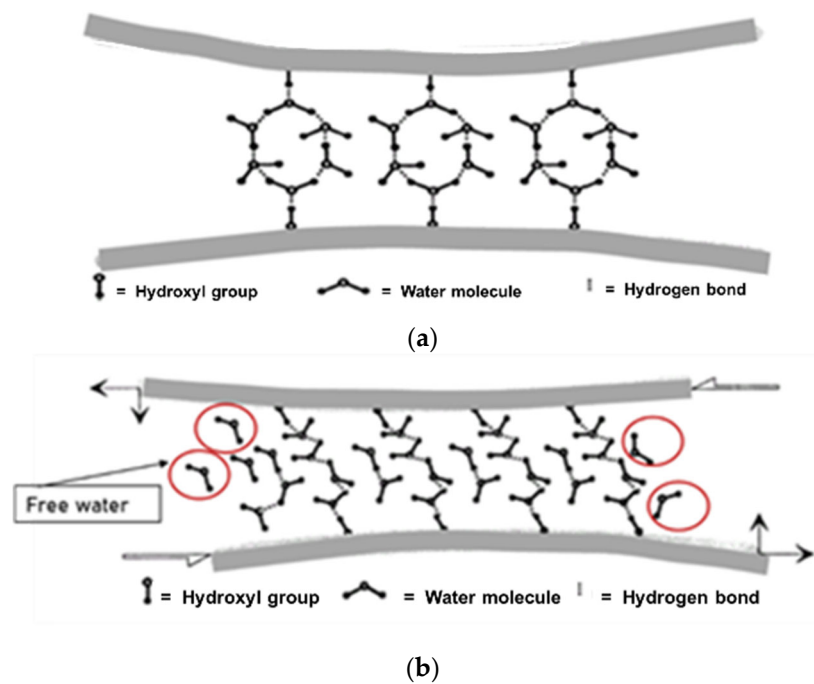
Figure 6. (**a**) C-S-H interlayer water structure. (**b**) Breaking of hydrogen bonds upon sliding between C-S-H sheets. Figure adapted from [36,37].

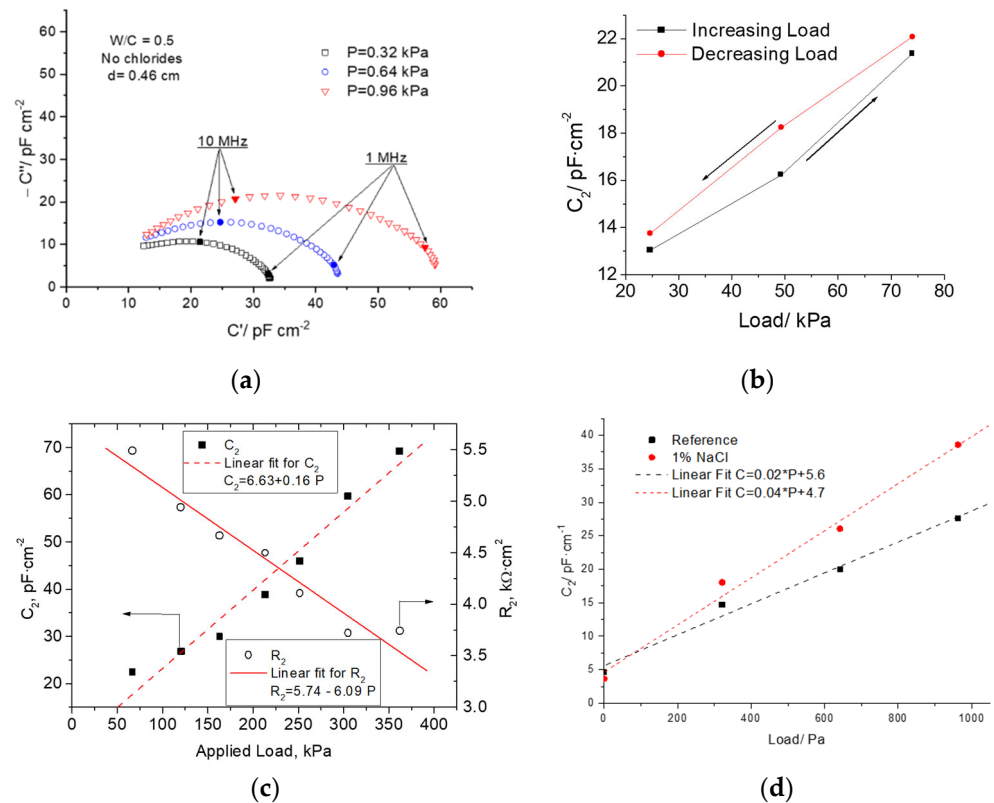**Figure 7.** (**a**) Dependence of the complex capacitance on the applied load. (**b**) Variation of C_2 parameter on a loading-unloading cycle (two minutes/cycle). (**c**) Dependence of the R_2 and C_2 parameters on the applied load. (**d**) Dependence of the C_2 parameter on the applied load for two cement chemistries, with and without chlorides. Figures (**b**,**c**) are taken from [38], Figures (**a**,**d**) from [39].

It is interesting to notice that the load ranges differ in Figure 7a,d and Figure 7b,c. The different ranges are due to the different microstructure of the cement paste prepared with Portland cement CEM I 52.5R with two different water/cement ratios, 0.5 in the former case, and 0.4 in the latter. As expected, the less porous structure (w/c = 0.4) has a higher Young modulus and shows elastic deformation at higher loads.

The cement chemistry affects the microstructure and thus the mechanical properties, as shown in Figure 7d, where the slope (dependence of C_2 in Figure 2c on the applied load) increases in the presence of chlorides in the cementitious mix.

Figure 7c shows the dependence of both parameters, R_2 and C_2, in Figure 2c, on the applied load. The dependence of R_2 is higher (higher sensitivity for a sensor) than that of C_2 due to the soluble salts that increase conductivity. The higher decreasing rate of R_2 compared with the increasing rate of C_2 causes the R_2C_2 time constant to decrease as the load increases, i.e., the characteristic frequency ($f_c = 1/2\pi R_2 C_2$) increases, and the Nyquist plots as in Figure 7a tend to rotate clockwise.

4.1.2. Relative Humidity Sensing

Perhaps the most evident sensing use of cementitious materials is as RH sensors owing to their porous nature, for which the Kelvin law (Equation (5)) applies.

$$Ln\left(\frac{P}{P_s}\right) = -\frac{M}{\rho RT}\frac{2\gamma}{r} \tag{5}$$

In Equation (5), P corresponds to the water vapor pressure at temperature T, and P_s corresponds to the saturation pressure at temperature T. Thus, the quotient is the RH in the bulk material, usually measured in the atmosphere of a hole drilled for that purpose. M is the molar mass of water, ρ its density, R the gas constant, and T the absolute temperature. γ is the surface tension and r the maximum pore radius for condensation to occur at vapor pressure P.

Although the pores are not cylindrical and the surface tension varies with the electrolyte concentration, a rough estimation of the pore sizes can be done. Taking $M = 0.018$ kg/mol, $\rho = 1000$ kg/m^3, $R = 8.31$ J/(K mol), $\gamma = 0.072$ J/m^2, and $T = 298$ K, for HR = 90% one gets that pores up to $r = 10.5$ nm will be water filled, while for RH = 50% r decreases to 1.5 nm.

The effect of water content on the sample's electrical properties is seen in Figure 8. Figure 8a shows the low-frequency limit of the capacitance plot decreases (thus, C_2 decreases) as the sample dries out because of the loss of water at the pore walls (and associated double layer capacitance). The individual pores contribute parallel to the global samples' electrical properties, so C_2 linearly decreases as pores dry out. However, the parallel contribution of the associated resistance (summing as the inverses) leads to the logarithmic dependence on drying shown in Figure 8b, making it highly sensitive and very useful to be used for sensing purposes. The R_2 dependence on the water content depicted in Figure 8b follows three distinct slopes associated with the different pore radii.

The different dependencies of R_2 and C_2 make the Nyquist spectra in Figure 8a rotate counterclockwise as the drying process progresses. Rotation is associated with the increased R_2 values that increase the R_2C_2 time constant and then decrease the associated characteristic frequency.
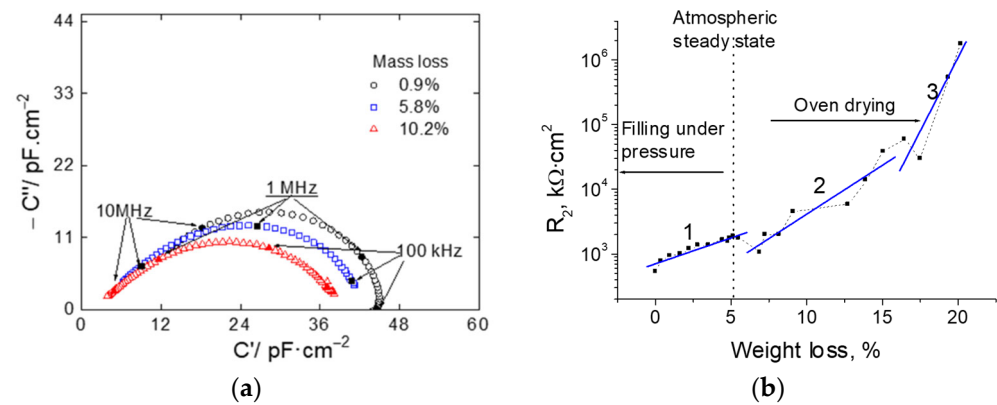
Figure 8. (**a**) Cole–Cole plot showing the dependence of the low-frequency capacitance limit with the water content of a cement paste sample. (**b**) Evolution of the R_2 resistance with the sample's water content. Figures taken from [29].

4.2. Reinforced Elements

A drawback of self-sensing cementitious materials is their low ductility, which limits their applicability under tension load. Several fillers have been tested that provide ductility [20] but also electrical conductivity due to the nature of the fillers employed: carbon-based and metal-based fillers (carbon fibers, carbon black, carbon nanotubes, graphite, graphene, steel slag, metal oxide, steel fiber, and nickel powder). When the filler concentration lies close to the percolation threshold (Figure 9a), any deformation of the material results in changing the spacing of the conductive filler, with associated changes in the measured resistivity [20,27,40].

For filler concentrations higher than the percolation threshold, the high electronic conductivity of the fillers short-circuits the ionic contributions to the impedance spectrum. However, for concentrations below the threshold, or for a non-contact measuring configuration, the only contribution of the embedded conducting fibers is that corresponding to their behavior as floating electrodes [41].
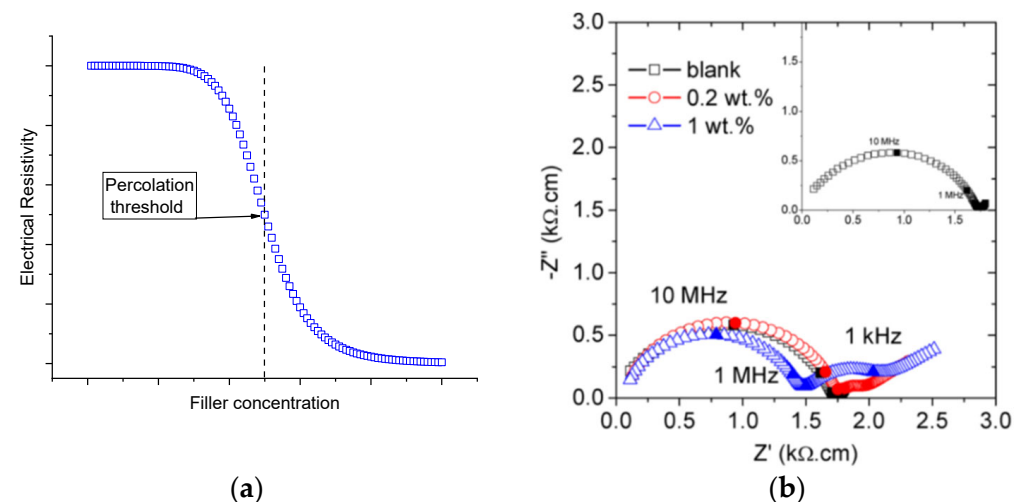

Figure 9. *Cont*.
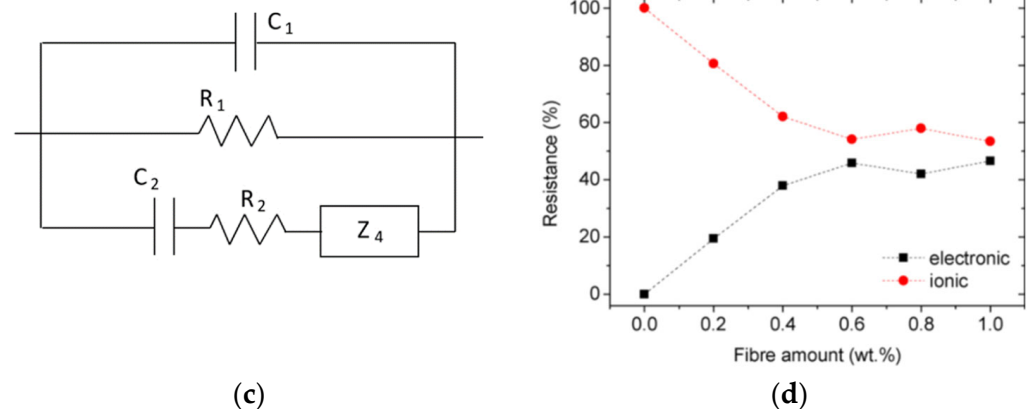
(c)

(d)

Figure 9. (**a**) Schematic representation of the dependence of the electrical conductivity on the conductive filler content. (**b**) High-frequency Nyquist impedance plots show the effect of the addition of carbon fibers. (**c**) Electrical equivalent circuit for fiber-reinforced samples at a concentration below the percolation limit. (**d**) Dependence of the ionic and electronic conductivities upon the fiber content. The figures are taken from [42,43].

Figure 9b depicts the effect of embedded floating fibers in the high-frequency impedance spectra of cement paste samples. The impedance decreases, and a new capacitive arc appears at around 1 kHz. The fibers represent a conducting interface that creates an interface with the surrounding liquid phase (in the cement pores) of high double layer capacitance. This new system was modelled adding, in the simplest case, a parallel R_4C_4 time constant to the R_2C_2 branch of the equivalent circuit in Figure 2c. The result corresponds to Figure 9c, where the element Z_4 accounts for the new time constant.

As the concentration of fibers remains in the case studied in [42] below the threshold limit, the only way for the fibers to drain current is via the exchange of ions with the non-percolating pores, represented by R_2C_2, thus, necessarily in series. This approach allows for differentiation between the electronic and ionic conductivities in the composite material, as shown in Figure 9d, by examining the ratio between the resistances present in the model. The dominant conduction can condition the type of application for a sensor.

The capacitance C_4 is also of great interest because it allows one to obtain an estimate of the degree of dispersion of the fibers. Moreover, it also can be used as a parameter for sensing because of its high absolute value (easy to measure) and its dependence on the fraction of wet fiber surface.

5. Conclusions

The origin of the electrical properties of porous cementitious materials and their use in self-sensing applications has been revised. The dependence that the electrical and/or ionic conducting properties of concrete and reinforced concrete elements have on the available free water makes them suitable for transductors in various sensing and self-sensing applications.

The water present in the cementitious matrix shows distinct dielectric behavior. The dielectric constant of water depends on its degree of binding via hydrogen bonds, which makes it valuable, via C_2 capacitance, for stress self-sensing.

The presence of fibers at concentrations below the percolation threshold limit increases the domain of self-sensing applicability because of the new interfaces formed.

Author Contributions: Conceptualization, B.D., X.R.N. and C.P.; literature review, C.P.; resources, X.R.N.; writing—original draft preparation, X.R.N.; writing—review and editing, B.D., X.R.N. and C.P.; and supervision, funding acquisition, X.R.N. All authors have read and agreed to the published version of the manuscript.

Data Availability Statement: Not applicable.

Conflicts of Interest: The authors declare no conflict of interest.

References

1. John, D.G.; Searson, P.C.; Dawson, J.L. Use of AC Impedance Technique in Studies on Steel in Concrete in Immersed Conditions. *Br. Corros. J.* **1981**, *16*, 102–106. [CrossRef]
2. McCarter, W.J.; Brousseau, R. The A.C. response of hardened cement paste. *Cem. Concr. Res.* **1990**, *20*, 891–900. [CrossRef]
3. Xu, Z.; Gu, P.; Xie, P.; Beaudoin, J.J. Application of A.C. impedance techniques in studies of porous cementitious materials. *Cem. Concr. Res.* **1993**, *23*, 853–862. [CrossRef]
4. Christensen, B.J.; Coverdale, T.; Olson, R.A.; Ford, S.J.; Garboczi, E.J.; Jennings, H.M.; Mason, T.O. Impedance Spectroscopy of Hydrating Cement-Based Materials: Measurement, Interpretation, and Application. *J. Am. Ceram. Soc.* **1994**, *77*, 2789–2804. [CrossRef]
5. McCarter, W.J. The fractal surface of cementitious materials determined by impedance spectroscopy. *Adv. Cem. Res.* **1994**, *6*, 147–154. [CrossRef]
6. Xie, P.; Gu, P.; Xu, Z.; Beaudoin, J.J. A rationalized a.c. impedence model for microstructural characterization of hydrating cement systems. *Cem. Concr. Res.* **1993**, *23*, 359–367. [CrossRef]
7. Keddam, M.; Takenouti, H.; Nóvoa, X.R.; Andrade, C.; Alonso, C. Impedance measurements on cement paste. *Cem. Concr. Res.* **1997**, *27*, 1191–1201. [CrossRef]
8. Ford, S.; Shane, J.; Mason, T. Assignment of features in impedance spectra of the cement-paste/steel system. *Cem. Concr. Res.* **1998**, *28*, 1737–1751. [CrossRef]
9. Mason, T.O.; Ford, S.J.; Shane, J.D.; Hwang, J.-H.; Edwards, D.D. Experimental limitations in impedance spectroscopy of cement-based materials. *Adv. Cem. Res.* **1998**, *10*, 143–150. [CrossRef]
10. Alonso, C.; Andrade, C.; Keddam, M.; Nóvoa, X.R.; Takenouti, H. Study of the Dielectric Characteristics of Cement Paste. *Mater. Sci. Forum* **1998**, *289–292*, 15–28. [CrossRef]
11. Nóvoa, X.R. Electrochemical aspects of the steel-concrete system. A review. *J. Solid State Electrochem.* **2016**, *20*, 2113–2125. [CrossRef]
12. Wang, R.; He, F.; Shi, C.; Zhang, D.; Chen, C.; Dai, L. AC impedance spectroscopy of cement—Based materials: Measurement and interpretation. *Cem. Concr. Compos.* **2022**, *131*, 104591. [CrossRef]
13. Díaz, B.; Guitián, B.; Nóvoa, X.R.; Pérez, M.C. The effect of long-term atmospheric aging and temperature on the electrochemical behaviour of steel rebars in mortar. *Corros. Sci.* **2018**, *140*, 143–150. [CrossRef]
14. Andrade, C.; Soler, L.; Nóvoa, X.R. Advances in Electrochemical Impedance Measurements in Reinforced Concrete. *Mater. Sci. Forum* **1995**, *192–194*, 843–856. [CrossRef]
15. Andrade, C.; Soler, L.; Alonso, C.; Nóvoa, X.R.; Keddam, M. The importance of geometrical considerations in the measurement of steel corrosion in concrete by means of AC impedance. *Corros. Sci.* **1995**, *37*, 2013–2023. [CrossRef]
16. Díaz, B.; Freire, L.; Nóvoa, X.R.; Puga, B.; Vivier, V. Resistivity of cementitious materials measured in diaphragm migration cells: The effect of the experimental set-up. *Cem. Concr. Res.* **2010**, *40*, 1465–1470. [CrossRef]
17. Keysight-Technologies. *Impedance Measurement Handbook. A Guide to Measurement Technology and Techniques*, 6th ed.; Application Note; Keysight Technologies: Santa Rosa, CA, USA, 2016.
18. Chung, D.D.L. Self-monitoring structural materials. *Mater. Sci. Eng. R Rep.* **1998**, *22*, 57–78. [CrossRef]
19. Han, B.; Ding, S.; Yu, X. Intrinsic self-sensing concrete and structures: A review. *Measurement* **2015**, *59*, 110–128. [CrossRef]
20. Han, J.; Pan, J.; Cai, J. Self-sensing properties and piezoresistive effect of high ductility cementitious composite. *Constr. Build. Mater.* **2022**, *323*, 126390. [CrossRef]
21. Lee, S.-J.; You, I.; Kim, S.; Shin, H.-O.; Yoo, D.-Y. Self-sensing capacity of ultra-high-performance fiber-reinforced concrete containing conductive powders in tension. *Cem. Concr. Compos.* **2022**, *125*, 104331. [CrossRef]
22. Chen, B.; Li, B.; Gao, Y.; Ling, T.-C.; Lu, Z.; Li, Z. Investigation on electrically conductive aggregates produced by incorporating carbon fiber and carbon black. *Constr. Build. Mater.* **2017**, *144*, 106–114. [CrossRef]
23. Cui, Y.; Wei, Y. Mixed "ionic-electronic" thermoelectric effect of reduced graphene oxide reinforced cement-based composites. *Cem. Concr. Compos.* **2022**, *128*, 104442. [CrossRef]
24. Han, B.; Yu, X.; Ou, J. Effect of water content on the piezoresistivity of MWNT/cement composites. *J. Mater. Sci.* **2010**, *45*, 3714–3719. [CrossRef]
25. Baeza, F.J.; Zornoza, E.; Andion, L.G.; Ivorra, S.; Garces, P. Variables affecting strain sensing function in cementitious composites with carbon fibers. *Comput. Concr.* **2011**, *8*, 229–241. [CrossRef]
26. Honorio, T.; Bore, T.; Benboudjema, F.; Vourc'h, E.; Ferhat, M. Dielectric properties of the pore solution in cement-based materials. *J. Mol. Liq.* **2020**, *302*, 112548. [CrossRef]
27. Zhang, J.; Heath, A.; Abdalgadir, H.M.T.; Ball, R.J.; Paine, K. Electrical impedance behaviour of carbon fibre reinforced cement-based sensors at different moisture contents. *Constr. Build. Mater.* **2022**, *353*, 129049. [CrossRef]
28. Díaz, B.; Nóvoa, X.R.; Pérez, M.C. Study of the chloride diffusion in mortar: A new method of determining diffusion coefficients based on impedance measurements. *Cem. Concr. Compos.* **2006**, *28*, 237–245. [CrossRef]

29. Cabeza, M.; Keddam, M.; Nóvoa, X.R.; Sánchez, I.; Takenouti, H. Impedance spectroscopy to characterize the pore structure during the hardening process of Portland cement paste. *Electrochim. Acta* **2006**, *51*, 1831–1841. [CrossRef]

30. Deus, J.M.; Díaz, B.; Freire, L.; Nóvoa, X.R. The electrochemical behaviour of steel rebars in concrete: An Electrochemical Impedance Spectroscopy study of the effect of temperature. *Electrochim. Acta* **2014**, *131*, 106–115. [CrossRef]

31. Feijoo, J.; Nóvoa, X.R.; Rivas, T. Electrokinetic treatment to increase bearing capacity and durability of a granite. *Mater. Struct.* **2017**, *50*, 251. [CrossRef]

32. Collazo, A.; Izquierdo, M.; Nóvoa, X.R.; Pérez, C. Surface treatment of carbon steel substrates to prevent cathodic delamination. *Electrochim. Acta* **2007**, *52*, 7513–7518. [CrossRef]

33. Cao-Paz, A.; Covelo, A.; Fariña, J.; Nóvoa, X.R.; Pérez, C.; Rodríguez-Pardo, L. Ingress of water into organic coatings: Real-time monitoring of the capacitance and increase in mass. *Prog. Org. Coatings* **2010**, *69*, 150–157. [CrossRef]

34. Vosgien Lacombre, C.; Bouvet, G.; Trinh, D.; Mallarino, S.; Touzain, S. Water uptake in free films and coatings using the Brasher and Kingsbury equation: A possible explanation of the different values obtained by electrochemical Impedance spectroscopy and gravimetry. *Electrochim. Acta* **2017**, *231*, 162–170. [CrossRef]

35. Artemov, V.G.; Volkov, A.A. Water and Ice Dielectric Spectra Scaling at 0 °C. *Ferroelectrics* **2014**, *466*, 158–165. [CrossRef]

36. Sierra, R. Répartition des différentes formes d'eau dans la structure des pâtes pures de C3S et de Ciment Portland. In Proceedings of the 7th International Congress on the Chemistry of Cement, Paris, France, 30 June–4 July 1980; Volume 3, pp. 201–206.

37. Feldman, R.F. Factors affecting young's modulus—Porosity relation of hydrated portland cement compacts. *Cem. Concr. Res.* **1972**, *2*, 375–386. [CrossRef]

38. Cabeza, M.; Merino, P.; Nóvoa, X.R.; Sánchez, I. Electrical effects generated by mechanical loading of hardened Portland cement paste. *Cem. Concr. Compos.* **2003**, *25*, 351–356. [CrossRef]

39. Cabeza, M.; Franco, M.; Izquierdo, M.; Nóvoa, X.R.; Sánchez, I. Effet des chlorures sur les propriétés chimiques et barrière de la pâte de ciment. In Proceedings of the 13ème Forum sur les Impedances Electrochimiques, Paris, France, 11 December 2000; pp. 43–53.

40. Wang, H.; Shi, F.; Shen, J.; Zhang, A.; Zhang, L.; Huang, H.; Liu, J.; Jin, K.; Feng, L.; Tang, Z. Research on the self-sensing and mechanical properties of aligned stainless steel fiber-reinforced reactive powder concrete. *Cem. Concr. Compos.* **2021**, *119*, 104001. [CrossRef]

41. Keddam, M.; Nóvoa, X.R.; Vivier, V. The concept of floating electrode for contact-less electrochemical measurements: Application to reinforcing steel-bar corrosion in concrete. *Corros. Sci.* **2009**, *51*, 1795–1801. [CrossRef]

42. Díaz, B.; Guitián, B.; Ramón Nóvoa, X.; Pérez, C. Conductivity assessment of multifunctional cement pastes by impedance spectroscopy. *Corros. Sci.* **2021**, *185*, 109441. [CrossRef]

43. Díaz, B.; Guitián, B.; Nóvoa, X.R.; Pérez, C. Analysis of the microstructure of carbon fibre reinforced cement pastes by impedance spectroscopy. *Constr. Build. Mater.* **2020**, *243*, 118207. [CrossRef]